Revealing corrosion parameters of steel in alkali-activated materials

Runci, Antonino; Provis, John; Serdar, Marijana

Source / Izvornik: **Corrosion science, 2023, 210(2)**

Journal article, Published version
Rad u časopisu, Objavljena verzija rada (izdavačev PDF)

Corrosion Science 210 (2023) 110849

Contents lists available at ScienceDirect

Corrosion Science

journal homepage: www.elsevier.com/locate/corsci

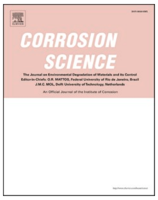

Revealing corrosion parameters of steel in alkali-activated materials

Antonino Runci [a], John L. Provis [b], Marijana Serdar [a,b,*]

[a] University of Zagreb, Faculty of Civil Engineering, Department of Materials, Croatia
[b] University of Sheffield, Department of Materials Science and Engineering, UK

ARTICLE INFO

Keywords:
Alkali-activated material
Corrosion
Chloride
EIS
Tafel

ABSTRACT

The long-term corrosion behaviour of reinforcing steel embedded in alkali-activated mortars (AAMs) prepared with three different binder compositions was monitored over a 360-day period by cyclic wetting/drying and spraying with chloride solution. Corrosion potential and polarisation resistance were determined by linear polarisation, individual resistance of mortar and steel by electrochemical impedance spectroscopy, and Tafel slopes by potentiodynamic anodic polarisation. The results were validated by correlating the electrochemical mass losses with the gravimetric mass losses. Based on the time evolution of the corrosion parameters, the study proposes new limits for passive and active corrosion conditions for reinforcing steel in AAMs.

1. Introduction

The penetration of chloride anions from seawater and/or de-icing salts into reinforced concrete is often the primary cause of the end of the service life of reinforced concrete. The accumulation of chloride anions at the interface between steel and concrete leads to the breakdown of the passive film and the progression of the corrosion process [1]. According to the model proposed by Tuutti [2], the corrosion process is divided into two phases: i) initiation phase and ii) propagation phase. In the first phase, the chloride anions penetrate through the pores of the concrete towards the interface between the steel and the concrete. Once the amount of chloride at the steel surface reaches the critical chloride content, c_{crit}, the depassivation of the steel begins [3]. In the second phase, the corrosion products are formed and the reaction propagates through the steel-concrete interface; the cross-section of the reinforcing steel decreases, and cracking/spalling may occur in the concrete. These processes lead to a premature end of the service life of a reinforced concrete structure [4,5]. The cost of preventing and mitigating the deterioration of reinforced concrete in the U.S. currently accounts for 3.1% of the gross domestic product (GDP) [6], and similar levels of economic damage are incurring in many developed nations. These costs could increase 3–6 times by 2060 and represent a significant economic challenge [7].

In this context, the development of new binders with longer durability than ordinary Portland cement (OPC) represents an important advancement in terms of economic and environmental impact. Among the available alternative binders, alkali-activated materials (AAMs) have a great potential for development and are widely considered as a promising alternative to OPC in many applications due to factors including the low carbon emissions associated with their production and their already demonstrated promising performance [8]. However, the difference between the reaction processes of AAM and OPC and the wide range of novel emerging compositions of AAMs make the current knowledge insufficient to guarantee long-term safety and reliability.

The protective passive film of iron oxides formed on the surface of steel embedded in a concrete is strongly influenced by the pH and chemical composition of the surrounding pore solution, as well as by the oxygen availability [9,10]. However, all three of these named factors can differ significantly in the case of OPC and AAM. The pH of AAMs is characterized by higher values than that of OPC, which is due to the high alkalinity of the activator. However, the absence of the buffering effect of $Ca(OH)_2$ as a reaction product may lead to an early decrease in pH due to the leaching of the pore solution and the carbonation process of the pore solution [11,12]. The variability of OH^- anion concentrations at the steel surface has a strong influence on the stability of the passive film [13,14].

In previous studies, it has been observed that partial or total replacement of OPC with blast furnace slag (BFS), even in slag-based AAMs, leads to a decrease in the redox potential of steel [15,16]. The change in redox potential is associated with the formation of a significant amount of reduced species, including HS^-/S^{2-} and $S_2O_3^{2-}$ [17]. However, the question arises as to how the presence of sulfides affects the corrosion behaviour of steel in slag-based composites and whether the lower observed redox potential of steel in such systems is due to

---

* Corresponding author at: University of Zagreb, Faculty of Civil Engineering, Department of Materials, Croatia.
E-mail address: marijana.serdar@grad.unizg.hr (M. Serdar).

https://doi.org/10.1016/j.corsci.2022.110849
Received 15 July 2022; Received in revised form 10 November 2022; Accepted 18 November 2022

Table 1
Chemical composition of the precursor materials, from XRF. All constituents are represented in fully oxidized form, regardless of oxidation state in the original materials.

Oxide composition (mass %)	SiO_2	Al_2O_3	Fe_2O_3	MnO	TiO_2	CaO	MgO	K_2O	Na_2O	SO_3
BFS_E	31.1	13.7	0.4	0.3	1.3	40.9	9.2	0.7	0	2.3
FA_P	57.2	25.1	5.8	0.05	0.9	4.8	1.7	1.5	1.1	0.8

corrosion activity, as is the case with OPC systems. On one side, it was recently observed that chemical reactions at the interface between steel and concrete involving sulfides protected the embedded steel from corrosion to some extent [18]. It was found that the sulfide species reacted with the passive film in tests using simulated pore solution, and produced FeS on the steel surface, changing the composition of the passive film [19–21]. According to this research, the onset of chloride-induced pitting corrosion on the steel surface depends on both sulfide concentration and exposure time. This is due to the change in the chemistry of the passive film in the presence of a strong reducing agent, which limits the corrosion rate at a sufficiently high sulfide concentration [20,22]. Conversely, a high sulfide concentration has also been argued to indicate a less well-developed passive film, since the oxidation of sulfide anions prevents or slows down iron oxidation, hindering the formation of an iron oxide layer around the reinforcement in the early stages of matrix development [23]. According to these findings, the passive film in the presence of sulfide can be characterized by a more porous structure compared to the one formed in OPC, which consists of an inner FeO and an outer FeOOH/Fe_2O_3 layer, making the steel more sensitive to corrosion in such instances [19]. Therefore, the influence of the chemical composition of the precursor, which consequently influences the chemical composition of the pore solution, on the corrosion parameters remains to be understood.

The stability of the passive film is also affected by the alkali concentration of AAMs [23]; as the alkali concentration increases, the c_{crit} increases, indicating a more stable passive film [20]. There is no apparent correlation between the silicate content of the AAM activating solution (denoted Ms, representing the molar ratio SiO_2/Na_2O in the activator), the type of alkali used, and the stability of the passive film [23]. The availability of oxygen at the interface between steel and concrete is also crucial to initiate both the passivation process and the corrosion process. A lack of O_2 can be caused by sulfide oxidation, which affects the redox potential [16], and the fine porosity and complex pore interconnection can cause low gas diffusion in AAMs, resulting in oxygen deficiency [24,25]. This parameter is strongly influenced by the precursors and the type and amount of activators used [26,27].

Most of the electrochemical parameters commonly used to monitor and describe the stability of the steel surface in cementitious materials are strongly influenced by the factors previously described. Among the most important one, corrosion rate (i_{corr}), which can be used to calculate reinforcement loss due to corrosion and confirm the stability of concrete structure, according to the Stern-Geary equation depends on measured steel resistivity and Tafel constants. The Tafel constants are affected by the conductivity of the electrolyte and polarization mechanism, which depend on the moisture content and chemical composition of electrolyte [28], and the pore structure of the concrete [29]. Measuring the appropriate value of the Tafel constant is an essential step in calculating the corrosion rate (in mm/year) from polarisation measurements. However, AAMs have shown great variability in pH and chemical conditions compared to OPCs [20,21,30], which can make it difficult to establish a single value for Tafel constants that applies to all types of AAMs.

In this paper, the time evolution of corrosion parameters of reinforcing steel embedded in alkali-activated fly ash, fly ash/slag, and slag mortar was monitored during 360 days of exposure to simulated marine environment in a salt spray chamber. The objective was to determine various electrochemical parameters as a function of the different concentrations of calcium, sulphide, and hydroxide (represented by pH) in the pore solution of the AAMs. Throughout the experimental period, the corrosion potential and polarisation resistance were regularly monitored by linear polarisation (LP), the individual resistances of mortar and steel were determined by electrochemical impedance spectroscopy (EIS), and the Tafel curves were determined by potentiodynamic anodic polarisation, under both passive and active conditions. At the end of the test period, corrosion was confirmed by analysis of the reinforcing steel, and the steel loss due to corrosion was calculated using gravimetric analysis. The objective of the study was to determine important corrosion parameters of steel in AAMs, to compare them with those commonly used for reinforcing steel in ordinary Portland cement, and to propose limits for distinguishing between passive and active corrosion conditions for reinforcing steel in AAMs.

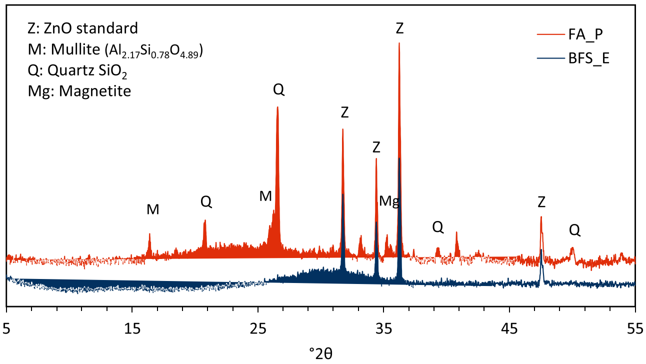

Fig. 1. XRD pattern of the precursor materials.

Table 2
Characteristic particle sizes and density of the precursor materials.

	$D_{v,\ 0.1}$, μm	$D_{v,\ 0.5}$, μm	$D_{v,\ 0.9}$, μm	Density, g/cm^3
BFS_E	1.3	4.9	10.6	2.89
FA_P	0.6	11.5	54.2	2.40

2. Materials and methods

2.1. Materials

A commercial ground granulated blast-furnace slag (BFS_E) supplied by Ecocem (Moerdijk, Netherlands), and a siliceous fly ash (FA_P) from coal-fired power station supplied by Lafarge Holcim (Plomin, Croatia) were used as solid precursors for mortar preparation. Table 1 shows the oxide compositions of the precursors, obtained by X-ray fluorescence spectroscopy. Fig. 1 shows the X-ray patterns of the precursors obtained by X-ray powder diffraction, with 10% ZnO as internal standard, using a CuKα radiation. The amorphous content of BFS_E was 100%, while FA_P contains 66.8% amorphous material, 16.4% mullite ($Al_{2.17}Si_{0.78}O_{4.89}$), 14.6% quartz ($SiO_2$), 2.4% anhydrite ($CaSO_4$), 1% magnetite ($Fe_3O_4$), 0.7% anhydrite ($CaSO_4$), and 0.4% free lime (CaO).

Particle size distribution (PSD) is a key parameter of precursors that affects the reactivity of the material as well as the consistency of the fresh mortar. PSD was determined by Mastersizer 2000 instrument (Malvern Panalytical, Malvern, United Kingdom) with a wet laser diffraction procedure by dispersing the particles in isopropanol along

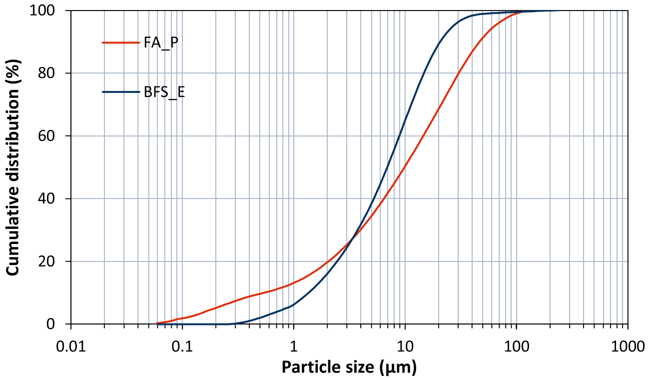

Fig. 2. Particle size distribution of the precursor materials, from laser diffraction.

Table 3
Mix design of the mortars tested in this study.

Mass (%)	SN3	BN3	FN9
BFS_E	87.67	41.12	0.00
FA_P	0.00	46.61	68.76
NaOH[a]	7.01	7.02	7.70
Na silicate (Ms 1.68)[a]	5.31	5.25	23.54
water/binder[b]	0.45	0.45	0.45
precursor/aggregate	0.33	0.33	0.33

[a] The activator content is referred to sum of liquid and solid component

[b] The water/binder includes also liquid and solid component from the activators.

with particle density [31]. Table 2 shows the density and characteristic values of particle size distribution, while Fig. 2 shows the cumulative distribution of particles of the precursors. The fly ash shows a bimodal distribution and larger particles with the bulk particle size around 20–30 µm, while the blast-furnace slag has finer particles, and the bulk particle size is around 10 µm. The higher amorphous content and the finer particle size indicates that BFS_E may have higher reactivity than FA_P.

The precursors were activated with sodium silicate Geosil 34417 from Woellner (Ludwigshafen am Rhein, Germany) with Ms = 1.68 (Ms or modulus ratio = $SiO_2/Na_2O + K_2O$), and with an NaOH solution of concentration 12.5 M. Technical grade sodium hydroxide pellets supplied by Grammol (Zagreb, Croatia) were dissolved in distilled water and mixed to prepare the NaOH solution 24 h before mortar preparation, enabling the solution to cool down before use.

2.2. Sample preparation

Table 3 summarises the mix designs of the AAM mortars tested in this study. SN3 and FN9 are based on blast furnace slag and fly ash, respectively, inspired by the mix designs tested recently by RILEM TC 247-DTA [32,33], while BN3 is a blended mortar, similar to SN3 but with 50% replacement of blast furnace slag by fly ash. All mixes were prepared with a water/binder ratio of 0.45 to achieve a suitable workability for sample casting. The aggregate was dolomite sand with a particle size range of 0–4 mm, and the precursor/aggregate mass ratio was 0.33 in all samples.

AAMs were prepared according to the recommended methods of RILEM TC 247-DTA [32,33]: the aluminosilicate precursor powder and aggregate were mixed for 60 s, and then again for 6 min while continuously adding activators and water (from the denser solution to the least dense); the mixing was paused for 60 s and then the mixture was mixed faster for 60 s. Samples were demoulded after one day of covered curing, and were then tightly wrapped with plastic film to prevent moisture loss and reactions with CO_2 (carbonation, efflorescence formation), for continued sealed curing until testing.

Table 4
Properties of alkali-activated mortar used for preparation of specimens.

Property	Standard (adapted where necessary to test AAMs)		SN3	BN3	FN9
Consistence (mm)	EN 1015-3		165	115	300
Air (%)	EN 1015-7		2.8	2.1	2.8
Compressive strength (MPa)	EN 196-1	7d	36	24.6	5.2
		28d	47.6	39.8	25.9
Apparent chloride diffusion coefficient (10^{-12} m^2/s)	NT BUILD 443		7.2	8.22	23.07
Migration coefficient (10^{-12} m^2/s)	NT BUILD 492		1.64	2.2	174
Total porosity (%)	Obtained by MIP [31]		4.59	18.19	13.9

2.3. Mortar characterization

The results of testing physical, mechanical and durability properties of the mortar used are shortly presented in Table 4. These properties were analysed in more detail in a previous paper by the authors [34]. It can be seen that FN9 has a poor resistance to penetration of chloride anions compared to OPC and other binders [35], while SN3 and BN3 provide high protection to chloride penetration despite their relatively high water contents [36,37].

2.4. Methods

The fresh mortar was cast into Ø5 × 10 cm plastic moulds that had smooth reinforcing steel bar placed in the middle (rebar dimensions were Ø0.6 ×8 cm), as shown in Fig. 3. (Table 5).

The smooth steel bars were ground to remove the upper layer with 400, 600 and 800 grit SiC until a homogenous shiny surface of the steel was reached, then cleaned with citric acid solution and dried with ethanol. A copper wire was soldered to the top of rebar to allow the connection to the rebar in the mortar during the electrochemical measurements. A thin layer of polymeric sealant paste was applied around the boundary to avoid galvanic and crevice corrosion.

After reaching 28 days of curing, the plastic film was removed; three samples per mix were exposed to tap water as reference cells at laboratory conditions (21 ± 3 °C), while three samples were exposed to an intense aggressive environment as corrosive cells in a salt spray chamber (Atlas, model S2000iS (Berwyn, USA)) according to ASTM B117. This test was carried out with a cyclic simulated tropical environment:

- Spray solution of 5%wt. NaCl at 20 ± 4 °C for 8 h,
- Saturation with 100% RH and 20 ± 4 °C for 24 h,
- Drying conditions at 50 ± 4 °C for 24 h.

An extra set of samples were corroded in a short time using a constant voltage to induce corrosion. The accelerated corrosion of the steel reinforcement was performed by imposing a constant voltage of 5 V to SN3 and BN3 for 60 h and 140 h to develop two levels of corrosion, and 3 V to FN9 for 9 h and 30 h. The chosen voltages were considered a compromise between short corrosion time and representation of environmental conditions, causing current densities under 200 μAcm^{-2} that correspond to the natural current density that would occur during corrosion of steel in concrete [38,39]. Current densities above 200 μAcm^{-2} would induce unrealistically high strain responses and influence chemical conditions at the steel-concrete interface area [40]. Fig. 4 shows a schematic representation of corrosion conditions and the electrochemical methods used during this study.

A conventional three-electrode cell was used to carry out the electrochemical measurements. The cell consists of a steel bar embedded in

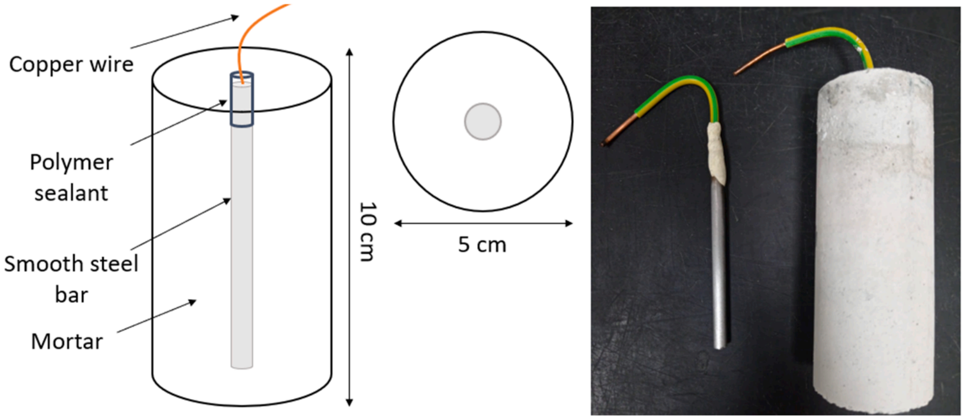

Fig. 3. Schematic representation of reinforced mortar used as working electrode.

Table 5
Chemical composition of reinforced steel used as working electrode.

Steel grade	Chemical composition, wt%											
	C	Mn	Si	P	S	Cu	Cr	Ni	N	Mc	V	CEV
1.0037 according to EN 10025–2	0.16	0.83	0.25	0.016	0.009	0.01	0.09	0.06	0.0051	0.016	0.005	0.33

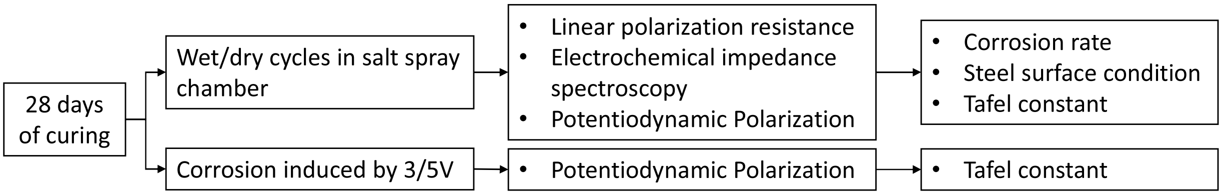

Fig. 4. Schematic representation of corrosion conditions, electrochemical characterization methods and aim of each method.

the cylindrical mortar specimen acting as working electrode (WE), a graphite rod as counter electrode (CE), and a saturated calomel electrode (SCE, SI Analytics, Mainz, Germany) as the reference electrode (RE). The electrochemical measurements were performed using a PAR VMP2 potentiostat/galvanostat (Biologic, Seyssinet-Pariset, France). The open-circuit potential (OCP) was measured constantly for 15 min to reach the stable E_{corr} value, after which the linear polarisation resistance (R_p) was measured. For the R_p measurements, the steels were polarised to ± 10 mV from the corrosion potential (E_{corr}) at a scan rate of 0.166 mV/s. Measuring the corrosion potential (E_{corr}) beforehand, R_p can be obtained from the slope of the polarization curve in the vicinity of E_{corr} [41]. The R_p is considered as a sum of resistances of the electrolyte solution, mortar and polarised steel without IR compensation, as described by Eq. (1):

$$E = E_{eq} + \eta + IR \tag{1}$$

where E_{eq} is the equilibrium potential defined by Nernst equation, η is overvoltage related to the exchanged current measured with respect to the equilibrium potential, and IR is the ohmic drop in the electrolyte solution and mortar. Here, it was considered that the electrical resistance of the testing solution and all mortars is equal for each set of samples (exposed to water and exposed to 5 wt% NaCl).

Once the polarisation resistance was measured, the corrosion current density (i_{corr}) was calculated using the Stern-Geary equation:

$$i_{corr} = \frac{(\beta_a \bullet \beta_c)}{2.3 \bullet R_p \bullet (\beta_a + \beta_c)} = \frac{B}{R_p} \tag{2}$$

where the B constant depends on β_a and β_c, the anodic and cathodic Tafel constants ($d\eta/dlogi$), respectively. The B constant is a fixed parameter, obtained by potentiodynamic polarization (PDP). The B constant is extrapolated from the slope of the anodic and cathodic branch of Tafel plots. A Tafel plot, which is a plot of log I vs. overpotential (E-E_{corr}), can be utilized to obtain both Tafel slopes and I_{corr} simultaneously by extrapolating the anodic and cathodic linear segments to an intercept of log I_{corr} through a curve fitting analysis [42]. However, PDP is considered a destructive test because the strong level of polarization can cause irreversible change in the working electrode. For this reason, B constant is a fixed parameter, which is conventionally estimated at 26 mV and 52 mV for active and passive states (respectively) of steel in a classical OPC concrete. These values are widely used in the corrosion rate estimation of steel in reinforced concrete [41]. However, the different chemical conditions at the steel-mortar interface in AAMs may induce variation of Tafel constants. For this reason, a limited number of specimens were tested and the data reported are the result of the average of two samples [43]. Therefore, the constants were extrapolated from the slope of the anodic and cathodic branch of Tafel plots at large overpotentials (E-E_{corr} $= \pm 200$ mV), with sweep rates between 2.5 and 10 mV/min in potentiodynamic polarization (PDP) as prescribed by Andrade et al. [44].

Electrochemical impedance spectroscopy (EIS) measurements were performed in a frequency range from 1 MHz to 1.58 mHz at the open circuit potential with ac perturbation ± 10 mV, with 5 points per decade.

Gravimetric mass loss measurements were performed in accordance with ASTM G1–03 [45] on specimens on which linear polarisation measurements were regularly performed, to validate the results of electrochemical mass loss calculated using the Stern-Geary equation. After splitting the mortar samples, the reinforcing bars were taken out and lightly cleaned with a brush, then immersed for about 20 min in a

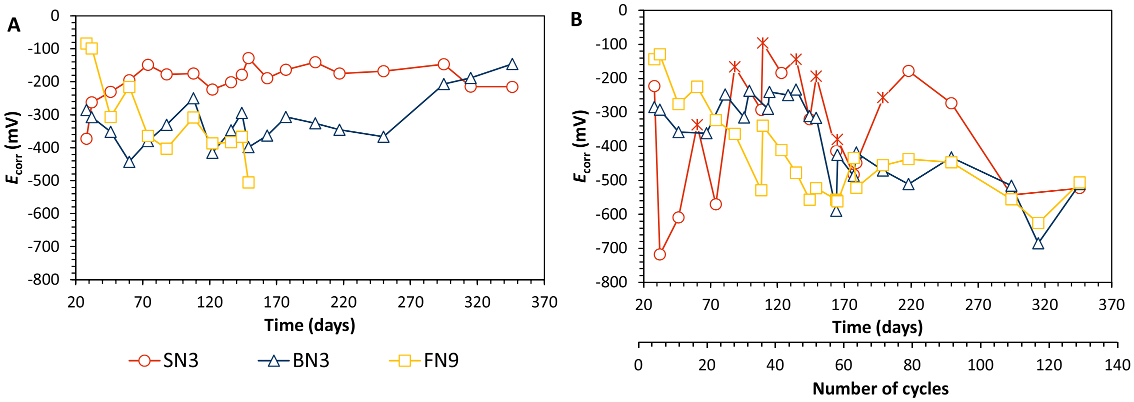

Fig. 5. Evolution of the potential values (**A**) as a function of time in reference cells and potential values (**B**) as a function of time in corrosive cells. In the corrosive cells (**B**), a dot indicates a measurement after dry period, while a x after a wetting time.

solution composed of 1000 mL hydrochloric acid (HCl 12.4 M), 20 g antimony trioxide (Sb_2O_3) and 50 g stannous chloride ($SnCl_2$). During the immersion, the cleaning solution was stirred, and the bars were removed from it alternatively, and lightly brushed to ease removal of the solidly adhered corrosion products. After treatment, all the bars were dried, and their masses were measured. The mass of the specimens after corrosion was subtracted from the original measured mass of the specimens before embedding in concrete to obtain the mass loss due to corrosion. The immersion and weighting procedures were repeated several times to obtain the mass loss as a function of the number of cycles for each bar. The mass loss corresponds to the point where the curve begins to flatten.

3. Results

3.1. Corrosion potential and polarization resistance

Fig. 5 shows the trends in E_{corr} values as a function of time, for SN3, BN3 and FN9 mortars in reference (tap water) and corrosive (chloride solution) cells. In the case of reference SN3, E_{corr} values increased up to − 150 mV, and stabilized after 60 days of exposure between − 150 to − 200 mV. These parameters are usual for passive conditions of steel in concrete according to ASTM C876–09 [46]. The reference cells of BN3 and FN9 showed fluctuating E_{corr} and R_p values. In reference FN9, E_{corr} values stabilized after 70 days around − 400 mV. E_{corr} values of reference BN3 oscillated around − 350 mV up to 250 days, after which the corrosion potential increased up to − 150 mV. For BN3 and FN9, the measured E_{corr} values correspond to conditions that would normally be taken to indicate active corrosion conditions according to usual limiting values for steel in Portland cement concrete [46]. For sample FN9, testing was stopped after 150 days because the sample showed cracks. For the other samples, testing continued up to 360 days.

In corrosive cells, the E_{corr} values were irregular and fluctuating because of wet/dry cycles; the measurements are indicated with a dot if taken after a dry cycle and with an asterisk if taken after a wet cycle. All systems showed that E_{corr} values increase after a wet cycle and decrease after a dry cycle, a trend which is in contrast with the trends demonstrated in the literature [47]. Saturated concrete conventionally shows a lower corrosion potential than dry concrete because of the lower oxygen availability at the steel-concrete interface [48]. The wet/dry cycles used in this study were limited to 24 h and this short time may not be sufficient to fully dry the core of a sample during the drying cycle and to saturate during the wetting cycle, convoluting the results, but this should still not be sufficient to fully invert the trend. Furthermore, the effect of wet/dry cycles could be hindered by the low porosity of some of the AAMs; SN3 showed the lowest porosity, and higher displacement in results between the wet and dry cycles.

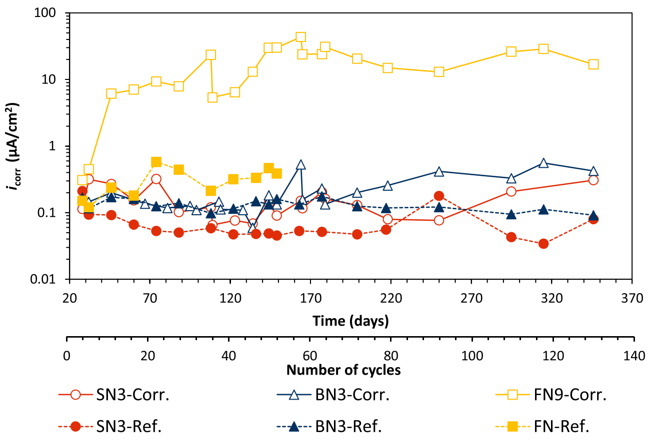

Fig. 6. Evolution of the current density i_{corr} versus the time of exposure in reference cells (circles) and corrosion cells (squares) for the different mortars.

SN3 and BN3 show similar behaviour: E_{corr} increased to − 200 mV and − 250 mV (respectively) after 70 days of curing, but after 220 days for SN3 and 300 days for BN3 E_{corr} decreased, and reached − 510 mV at 360 days in both samples. Conversely, E_{corr} of FN9 reduced constantly until reaching − 500 mV at 130 days.

Fig. 6 shows the current density (i_{corr}) of steel embedded in mortar exposed to reference (tap water) and corrosive (NaCl solution) environments. I_{corr} was calculated from the Stern-Geary equation, using the fixed values for B constant. In reference cells, the BN3 and SN3 i_{corr} values remained stable under 0.2 μA/cm^2, while the values for FN9 increased up to 40 μA/cm^2 after 160 days of exposure. In corrosive cells, both BN3 and SN3 showed low current densities of under 0.4 μA/cm^2, with a slight increase after 280 days. The current density of FN9 in the corrosive cell indicated early corrosion, with a current density value of 6 μA/cm^2 after 40 days and 30 μA/cm^2 at the end of the exposure period.

3.2. Electrochemical impedance spectroscopy

Fig. 7 shows phase shift for reinforced BN3 after 350 days of exposure in reference and corrosive environments. The high displacement of the low frequency range is coherent with the pitting process visible on the steel surface. Figs. 8–10 show Nyquist plots for steel embedded in alkali-activated mortars in reference and corrosion cells up to 300 days. The electrochemical impedance spectroscopy was performed to provide information related to the steel-concrete interface area, as well as to distinguish between the resistance of the mortar and of the reinforcing

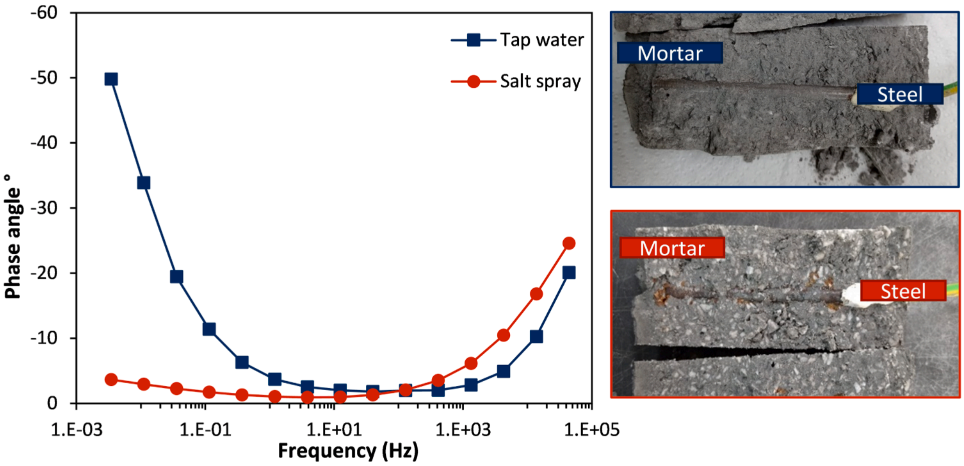

Fig. 7. Phase shift of reinforced BN3 mortar exposed to and visual examination of steel surface after 350 days of exposure.

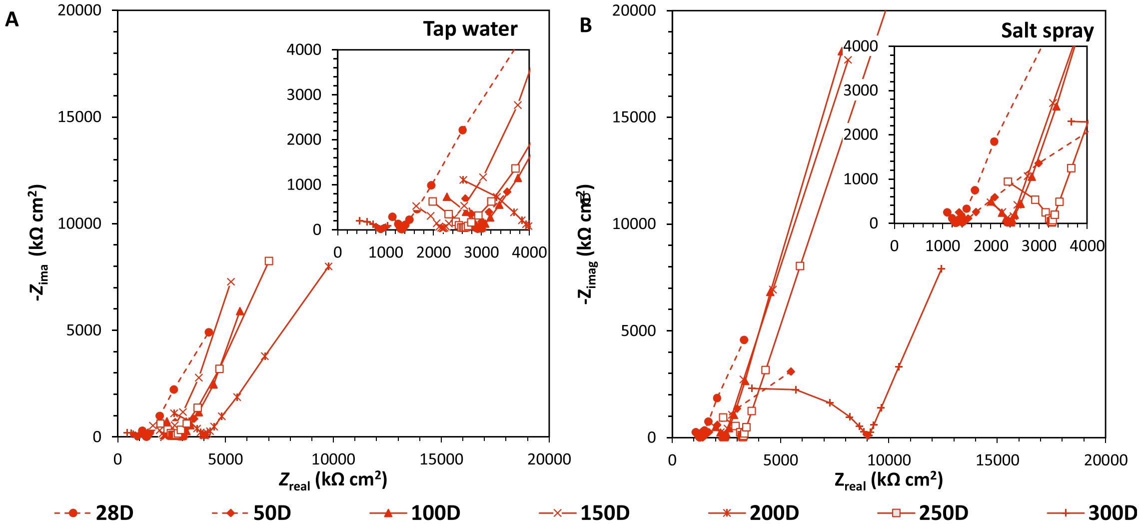

Fig. 8. Nyquist plots of SN3 mortar reinforced in tap water (A) and in salt spray chamber (B) after different exposure times.

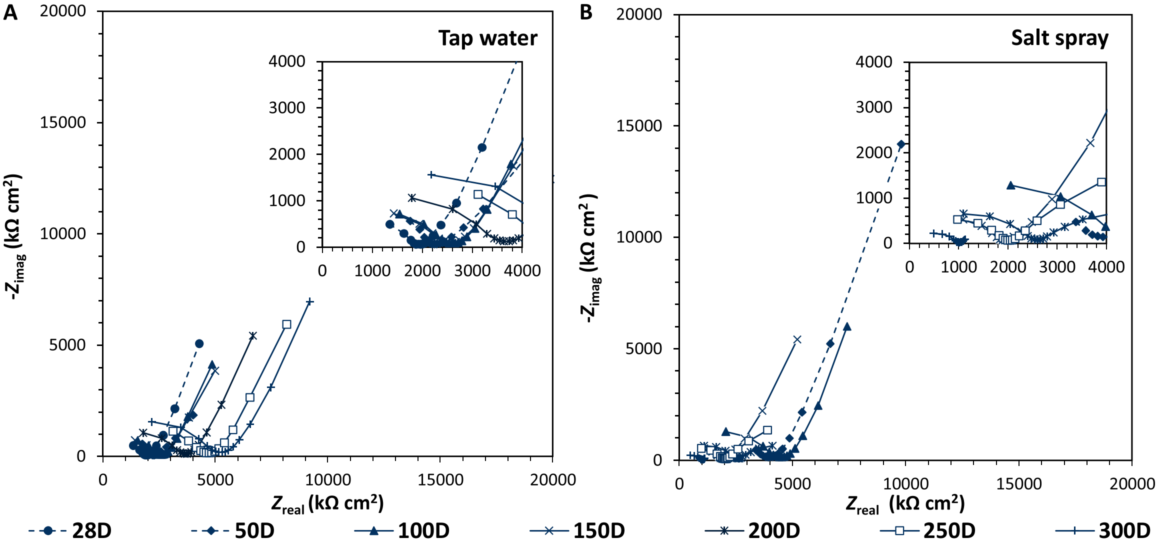

Fig. 9. Nyquist plots of BN3 mortar reinforced in tap water (A) and in salt spray chamber (B) after different exposure times.

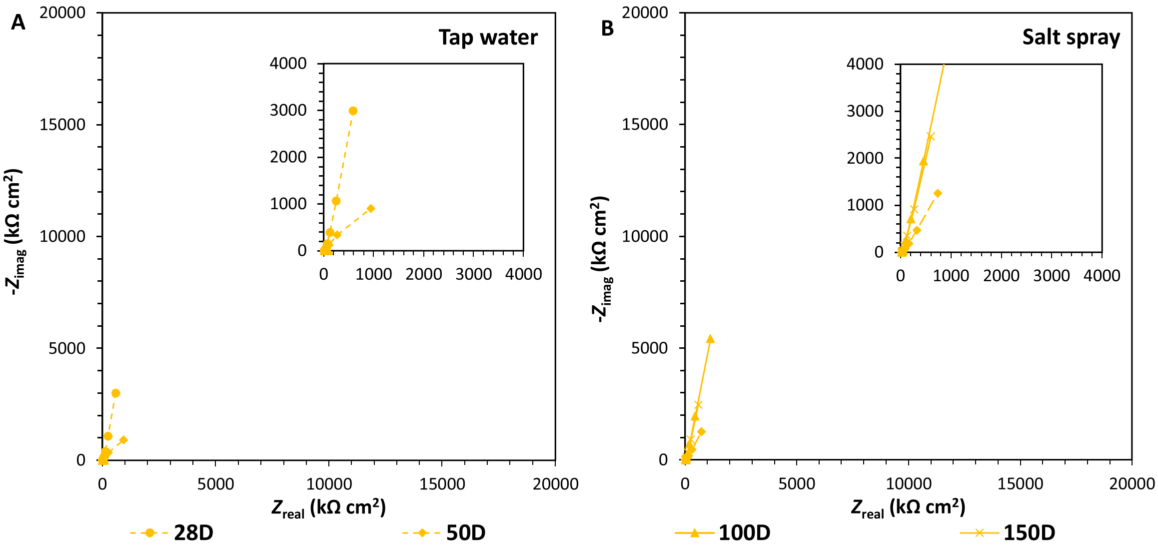

Fig. 10. Nyquist plots of FN9 mortar reinforced in tap water (A) and in salt spray chamber (B) after different exposure times.

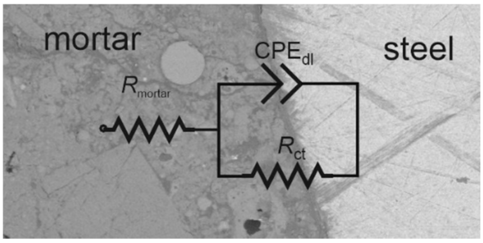

Fig. 11. Equivalent electrical circuit (EEC) used in fitting impedance spectra for AAMs mortars.

steel.

The impedance data were fitted using a simple electrical equivalent circuit (EEC) shown in Fig. 11. The EEC used is characterized by the electrolyte and mortar resistance obtained in the high frequency range, R_{mortar} [49], while the lower frequency range is associated with the steel/electrolyte interface (CPE_{dl}/R_{ct}) [50]. To ensure quality of fitting, fitting error was kept under 10% for all obtained parameters.

The steel/mortar interface is described by a combination of charge transfer resistance, R_{ct} and double layer capacitance, CPE_{dl}, at the steel-mortar interface (SMI) and reflects the corrosion resistance of the steel surface being controlled by the properties of passive film. In the proposed circuit, a frequency-dependent constant-phase element (CPE) was introduced instead of a pure capacitance, to account for the inhomogeneities present in the mortar structure [51,52]. The impedance of a constant-phase element is defined as $Z_{CPE} = [CPE(j\omega)^n]^{-1}$, where the deviation of the CPE from pure capacitance is characterized by the exponent n, which ranges from 1 for pure capacitance to 0 for non-capacitance [52–54]; j is the imaginary unit ($j^2 = -1$); and ω is the angular frequency (2πf, where f is the frequency). The exponent of the constant-phase element (n) is related to the degree of the surface heterogeneity of steel-mortar interface for CPE ($n = 1$ for a highly homogeneous surface, which then represents a pure capacitor) [52,54].

Table A1 shows the evolution of the electrolyte and bulk matrix resistances (R_{mortar}) as a function of time for mortars. In the reference cells, R_{mortar} is stable beyond 50 days of reaction, indicating that C-A-S-H and N-A-S-H gels develop, and pore refinement and evolution of pore fluid chemistry becomes more limited, so is not visible in the EIS parameters [51]. Furthermore, the higher resistance of SN3 compared to the other systems is coherent with the chloride diffusion results reported in Table 4 [23,37,55]. While R_{mortar} increased regularly up to 336 kΩ cm^2 in BN3 and showed a dramatic increment from 212 to 520 kΩ cm^2 in SN3, after 300 days. In corrosive cells, R_{mortar} of SN3 increased up to 268 kΩ cm^2 at 250 days, and R_{mortar} of BN3 increased up to 253 kΩ cm^2

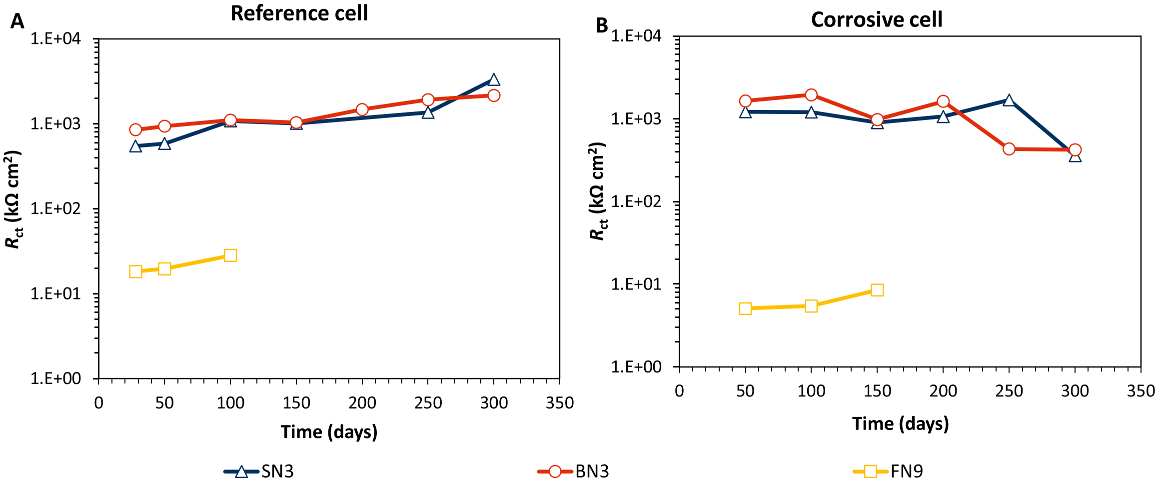

Fig. 12. Comparison of the charge transfer resistance (R_{ct}) in tap water (A) and in salt spray chamber (B).

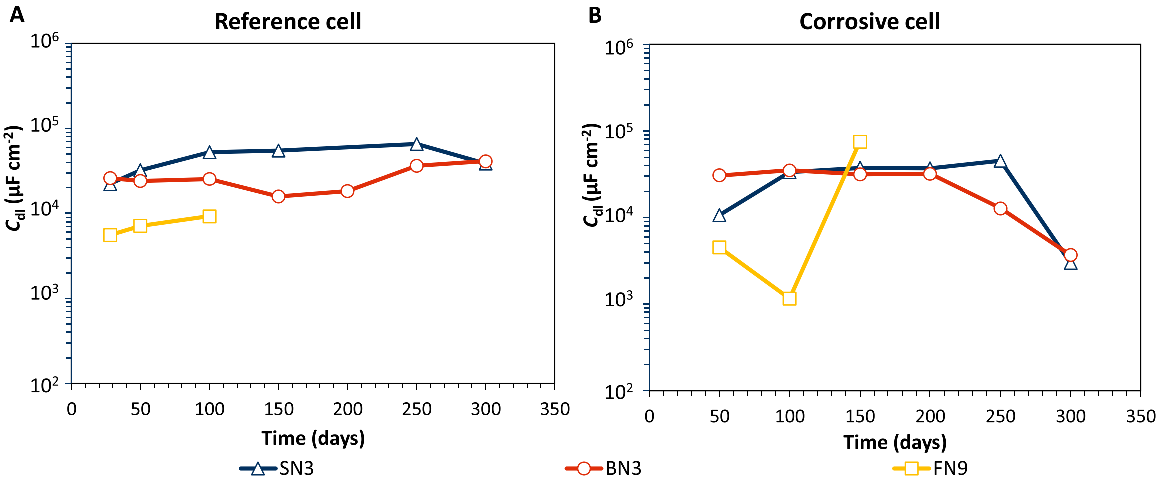

Fig. 13. Comparison of the double layer capacitance (CPE_{dl}) at mortar-steel interface area in tap water (A) and in salt spray chamber (B).

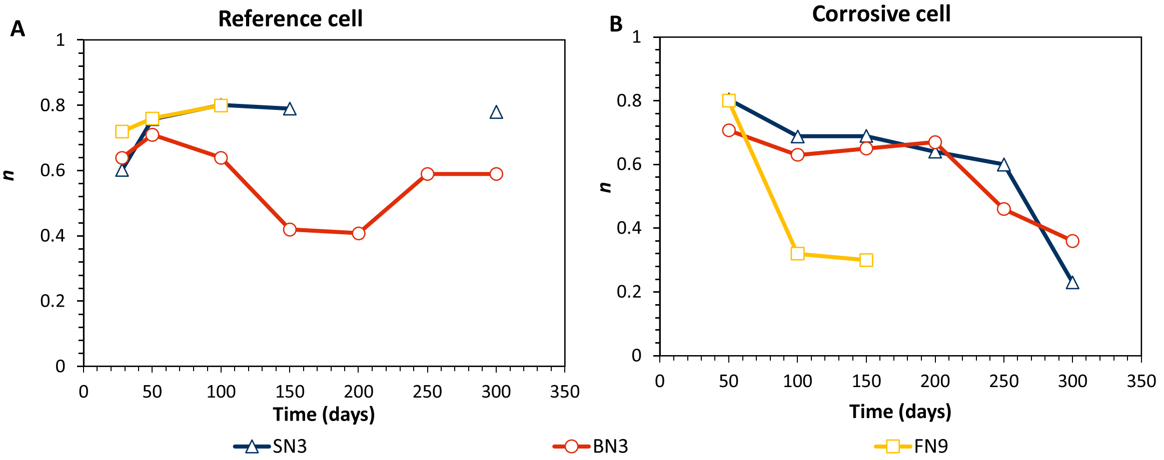

Fig. 14. Comparison of the exponent of CPE (n) parameter at mortar-steel interface area in tap water (A) and in salt spray chamber (B).

at 200 days. Despite this stability R_{mortar} of both moves to 55 kΩ cm^2 for SN3 and 66 kΩ cm^2 for BN3. This lowering trend is probably connected to the cracking process of the mortar layer due to the corrosion product growing on the steel surface [56–59]. In the case of FN9, R_{mortar} was stable at ~1 kΩ cm^2 in reference and corrosive cells, indicating lower resistance of mortar in both environments.

Table A1 and Figs. 12–14 display the evolution of steel-mortar interface charge transfer resistance (R_{ct}) and double layer capacitance (C_{dl}), and the parameter n, as a function of time for mortars under the reference and corrosive environments. The double layer capacitance, C_{dl} in μF cm^{-2}, was calculated using the constant-phase element values, CPE, the exponent n, and the resistances, R_{mortar} and R_{ct}, according to Brug's formula [53,63]. In reference cells of BN3 and SN3, R_{ct} continuously increased during the exposure, and reached 3335 kΩ cm^2 for BN3 and 2153 kΩ cm^2 for SN3 after 300 days of exposure. R_{ct} was higher in BN3 than SN3, which may be linked to the different electrochemical response of passive film in blast-furnace slag based-systems due to the formation of a sulfidic layer [11,20], which is stronger in SN3 than BN3. The significant increase of resistance after 100 days may be connected to the oxidation of HS$^-$ and changes in the passive film structure [14,18,56], suggesting an increase in passive film thickness and protection from corrosion. Similar trends are shown in the n results, where SN3 has a stable value ~0.8 after 100 days and BN3 ~0.6 after 250 days, indicating higher homogeneity and stability in the SN3 passive film.

In the corrosive environment, R_{ct} of both SN3 and BN3 decreased after 250 days of exposure, reaching a value 385 kΩ cm^2 and 424 kΩ cm^2, respectively. This trend indicates passive film breakdown and corrosion process development, which is followed by the heterogeneity of the steel surface increase, causing reduction of n, according to the trend observed in R_{ct}. The double layer capacitance is stable between 20 and 60 mFcm^{-2} in both reference and corrosive environments during initial testing period. It is interesting to notice that the double layer capacitance was increasing in the case of SN3 during the initial exposure, indicating higher activity in the passive film. The capacitance variations are small in the reference environment and corrosive environments after 50 days, indicating that the area at the steel-mortar interface is stable [60]. However, C_{dl} decreased in the corrosive environment to 3 in SN3 and 3.7 mFcm^{-2} in BN3 after 300 days. These values are coherent with the trends in resistance and may indicate that pitting corrosion processes in the steel-mortar interface area leads to the development of corrosion products [14,51].

FN9 showed different behaviour from the blast furnace slag-based systems. For this sample, R_{ct} had low values between 5 and 10 kΩ cm^2 in both reference and corrosive environments, indicating lower degree of passive film development. The C_{dl} values of the reference cells results were higher than SN3 and BN3, indicating that FN9 shows higher porosity in the steel-mortar interface area compared to the other systems. C_{dl} values in the corrosion cell for FN9 first decreased and soon after abruptly increased, indicating partial filling of the steel concrete interface with corrosion products [14]. Since the corrosion products formed by pitting corrosion are porous, the significant increase in double layer capacitance after the onset of pitting corrosion can be

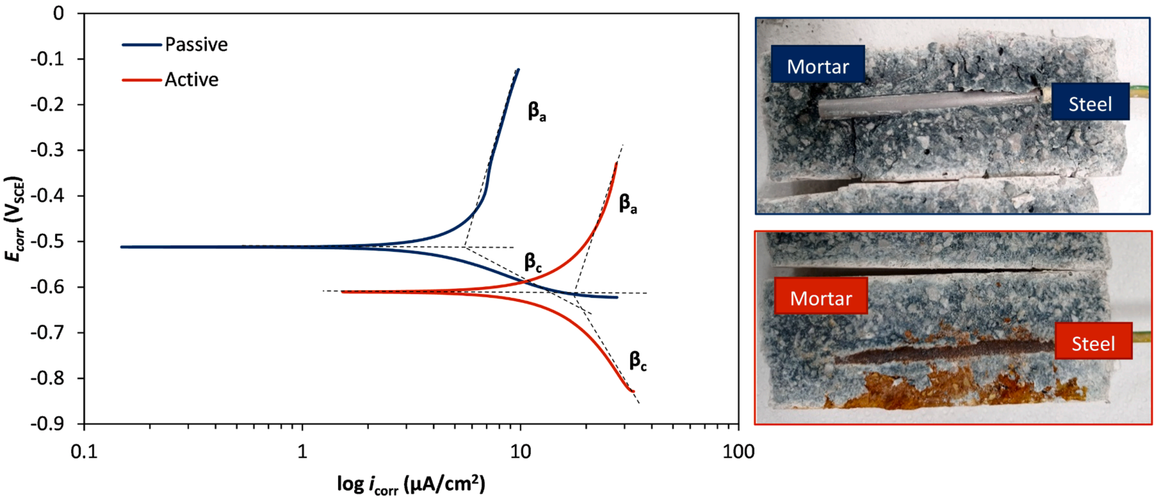

Fig. 15. Example of polarization curves for passive and active SN3 samples, obtained by potentiodynamic polarization $E\text{-}E_{corr} = \pm 200$ mV, with sweep rates between 2.5 and 10 mV/min, and visual examination of steel surface at the end of measurement.

attributed to the increase in surface roughness caused by pitting corrosion and the accumulation of corrosion products [53,61]. The parameter *n* decreased progressively after 250 days in SN3, 200 days in BN3 and 100 days in FN, indicating the growing of heterogeneity on the steel surface due to the breakdown of passive films and pitting corrosion initiation [57,62].

3.3. Tafel constant

The Tafel constants are crucial for calculation of corrosion current density by the Stern-Geary equation. They are obtained from the extrapolation of the anodic and cathodic branches of the polarization curves applying a large overpotential above the corrosion-free potential ($\Delta E = \pm 250$ mV) [41]. The "Tafel extrapolation" is a destructive approach, and for this reason it is preferred to calculate the corrosion current density by LPR. LPR allows the calculation of corrosion current density using defined Tafel constants. The most common constants were defined by Andrade and Gonzalez [64]: reinforced mortar based on OPC provides 120 mV/decade for both β_a and β_c, corresponding to a B constant equal to 26 mV for passive conditions and 52 mV for active conditions. These results have been proven by gravimetric analysis and are widely used as main inputs for corrosion monitoring of conventional reinforced concrete structures. However, the polarisation behaviour of reinforcement in fly ash and slag cement concretes may induce higher β_a and β_c values compared to those proposed by Andrade and Gonzalez [64], and it may not be possible to identify a constant value for B [65,66]. Indeed, Garcés et al. [67] have already demonstrated that the value of B may fluctuate based on pH and the presence of chloride anions, even for Portland-based cements.

The values of Tafel slopes and the B constant may be affected by: the conductivity of the electrolyte which depends on the moisture content and presence of various ions such as Cl^-, the pH of the electrolyte that can be affected by the carbonation or chemical composition of the electrolyte, the polarisation mechanism (i.e. activation polarisation or concentration polarisation) which depends on the availability of the ions involved in redox reactions [28], and the pore structure of the concrete which influences the oxygen transportation till the steel surface [29]. Although chemical composition of the binder (which defines the electrolyte composition of the pore fluid) is only one of the many parameters which affect the corrosion kinetics, AAMs have demonstrated wide diversity in pH and chemical conditions at the steel/concrete interface area compared to OPC [20,21,30], which may influence Tafel constant values. Thus, measuring the Tafel constants is an essential step to enable the calculation of corrosion current density and resulting corrosion rate of reinforcing steel in AAMs.

Table 6
Cathodic and anodic Tafel constants for passive and active samples.

Mix	P_{corr}, μm	E_{corr}, mV	β_a, mV/decade	β_c, mV/decade	*B*, mV
FN9	2.64**	-404	21.2	996.8	40
	5.98	-665	40.4	301.7	13.1
	6.36	-657	493.9	348	37.2
	7.88	-851	837.7	526.4	48.2
	15.7*	-469	530.5	202.8	63.8
BN3	0.2**	-500	457.7	39.9	16
	0.4**	-331	564.2	35.7	14.6
	0.65**	-278	508.1	38.9	15.7
	0.78*	-402	1248.1	87.8	35.4
	1.1	-386	313.3	274.5	63.6
	1.9	-665	270.4	234.6	54.6
	1.72*	-683	244.5	147.1	39.8
	2.18*	-386	313.3	274.5	63.6
	2.63*	-665	270.4	234.6	54.6
SN3	0.66**	-541	359.2	127.2	40.8
	0.77**	-402	541.	64.4	25
	1.7	-523	718.5	81.8	31.9
	1.8*	-674	243.2	223.8	50.6
	2.4*	-738	256.4	243.9	54.3

[*] Corrosion process induced by constant voltage.
[**] Passive condition 3 s.

Fig. 15 shows the polarisation curve for active and passive condition of steel embedded in AAMs. Curve-fitting analysis using the least-squares (χ^2) method was performed to calculate β_a and β_c based on the slopes in the anodic and cathodic linear sections of the fitted curves [43]. Subsequently, the B Tafel values were determined following Eq. (1).

Table 6 reports the values of the Tafel constant for steel embedded in AAMs. Constants were obtained for steel at different stages of corrosion propagation, which are expressed by the corrosion propagation, P_{corr}, in μm, calculated according to Eq. (3):

$$P_{corr} = \frac{11.6 \times i_{corr} \times t}{365} \tag{3}$$

Where i_{corr} is the corrosion rate (μA/cm^2), 11.6 is a conversion factor and *t* is the time (days) [68]. The different stages of corrosion propagation were achieved either by prolonged exposure to cycles in the salt spray chamber and/or by applying a constant voltage to accelerate corrosion (values obtained by impressing voltage are indicated with an asterisk in the Table). Fig. 16 shows the evolution of B constant

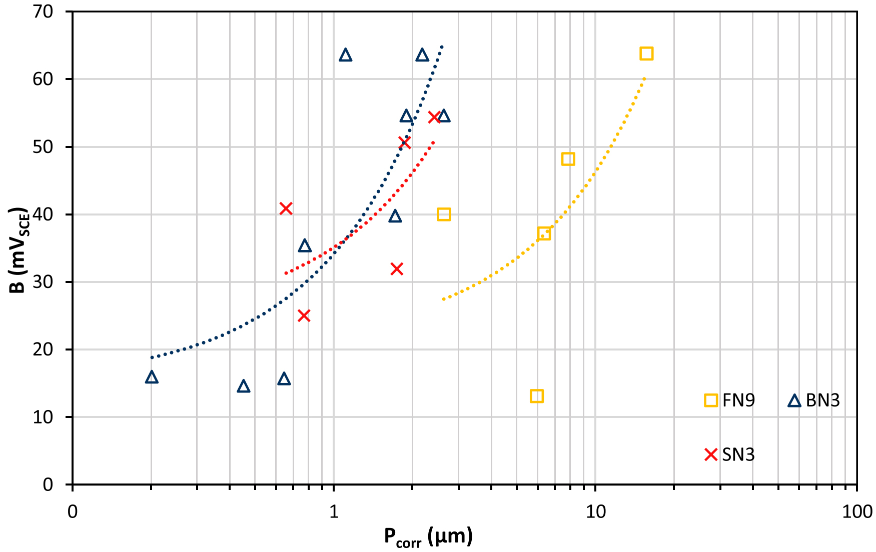

Fig. 16. Correlation between corrosion depth (P_{corr}) and B constant.

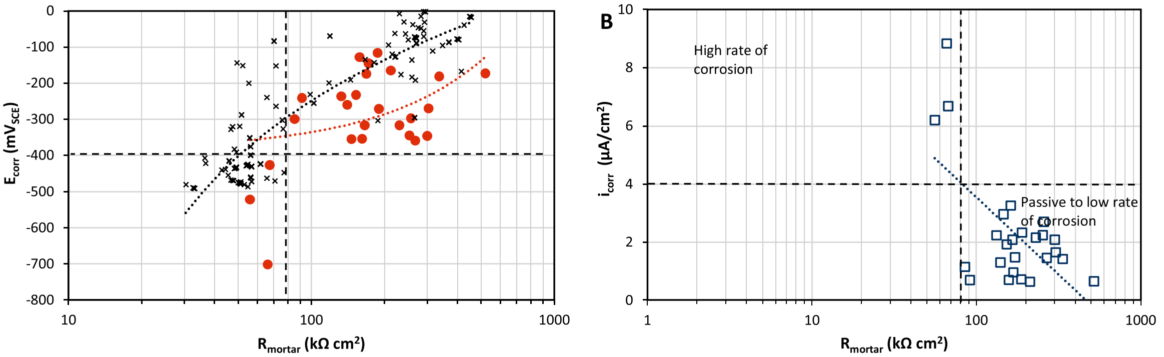

Fig. 17. Relationships between half-cell potential (E_{corr}) and mortar resistance (R_{mortar}) obtained by EIS fitting, compared with results obtained by Elsener et al. [48] for OPC (**A**), and relation between mortar resistance (R_{mortar}) and corrosion rate (**B**).

depending on the phase of corrosion propagation, and on the type of precursor in AAM. Increasing the corrosion propagation, B constant increased, moving away from the reference data defined for OPC. SN3 and BN3 had respectively $B \approx 25$ mV and ≈ 15 mV for passive conditions, and $B \approx 54$ mV and ≈ 55–63 mV for active conditions. On the other side, FN9 showed irregular path, revealing dramatic increase in B constant with increase of corrosion depth. The results presented here for BN3 are consistent with the work of Babaee and Castel [23],

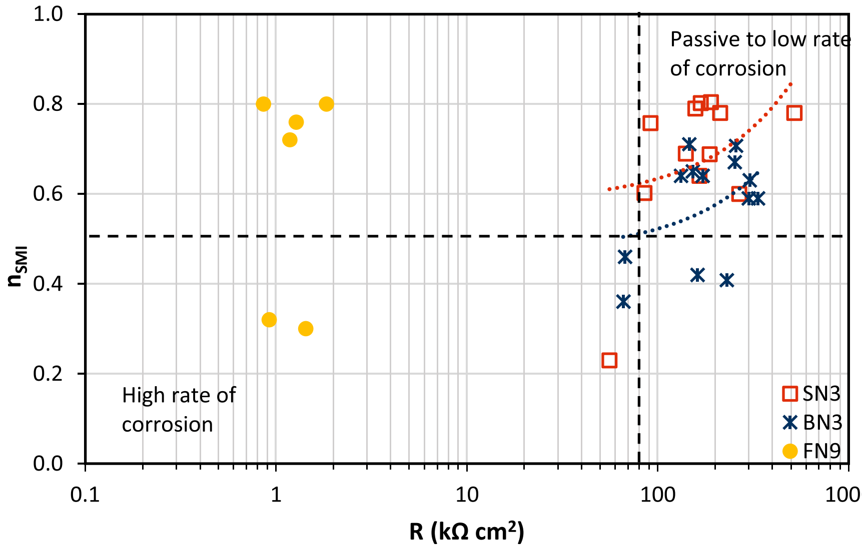

Fig. 18. Relation between the exponent of CPE (n) and mortar resistance (R_{mortar}) obtained by EIS fitting.

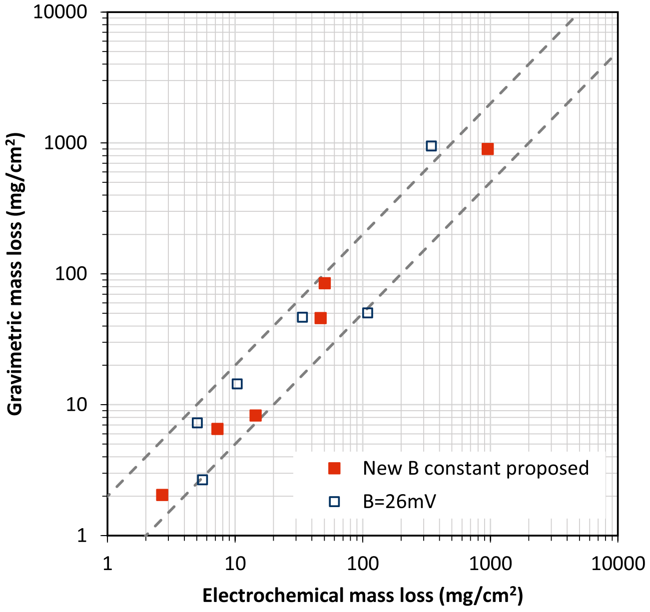

Fig. 19. Gravimetric mass loss vs. electrochemical mass loss for AAMs when using B constant proposed for OPC [64] (blue empty squares) and new B constant proposed for AAMs in current work (red full squares). The dotted lines indicate the range of acceptance for correlation defined by Andrade and Gonzalez for OPC [64].

who demonstrated that in alkali-activated fly ash, blended with low concentrations of blast furnace slag and metakaolin, the "B" constant shows similar trends and values to BN3 here, with B ≈ 15 mV for passive conditions, and B = 65–45 mV under active conditions moving from low to high corrosion rate.

4. Discussion

As was demonstrated by LPR results in the Section 3.1, the use of E_{corr} in isolation can be a misleading parameter for corrosion identification due to the crucial influences of HS^- concentration, O_2 availability and wet/dry cycles. An alternative parameter that can indicate corrosion risk in the case of chloride anions penetration is mortar resistance [69,70], which describes the mortar ability to withstand the transfer of charge [29]. The corroded steel usually coincides with low resistance areas, indicating higher chloride anion penetration, thus more open pores [70]. Fig. 17. A shows the correlation between the steel potential (E_{corr}) and mortar resistance (R_{mortar}) obtained by EIS fitting from this study (red dots), as well as the same correlation for OPC from the literature [48] (black cross). The mortar resistance is less affected by humidity and oxygen availability than E_{corr} and it is possible to define limits of passive and active condition. Compared to the data of Elsener et al. [48] for Portland cement, the results obtained here for AAMs are shifted to lower E_{corr} and higher mortar resistance values.

Fig. 17. B shows the correlation between the current density (i_{corr}) obtained by linear polarisation and mortar resistance (R_{mortar}) obtained by EIS fitting. The correlation is not precise, but general trends can be observed and analysed. Reducing the mortar resistance, the corrosion rate increase, while E_{corr} was not always coherent with R_{mortar} results. Furthermore, it is possible to identify regions of passive and corroding conditions, which are shifted to lower E_{corr} values compared to observations in OPC [48]. Mortar resistance may be used to broadly identify steel conditions and may be a valid tool for indirect measurement as an alternative to E_{corr} monitoring [29]. Regardless of the fact that mortar resistance can be strongly influenced by the chemical composition of the systems, especially OH^- concentration [69], the results presented for AAMs show a visible distinction between high corrosion activity area and passive or negligible corrosion activity.

Table 7
Proposed values of corrosion potential (E_{corr}), mortar resistance (R_{mortar}), the exponent of $\mathrm{CPE_{dl}}$ (n) and Tafel constant B for passive and active steel in AAMs.

Risk of corrosion	E_{corr} ($\mathrm{mV_{SCE}}$)	R_{mortar} ($\mathrm{k\Omega \cdot cm^2}$)	n (dimensionless)	B (mV)
Passive or negligible corrosion conditions	> -400	> 80	> 0.6	15–25
Corrosion conditions	< -400	< 80	< 0.6	55–63

Another EEC parameter that is indicative of the steel surface conditions is the exponent of the constant-phase element (n), that reflects the degree of the surface heterogeneity [54]. Fig. 18 shows the correlation between n and the mortar resistance (R_{mortar}) obtained by EIS fitting. Fig. 18 shows that in corrosive environments, n indeed generally decreases in a similar manner to the mortar resistance, thus reflecting the increase in surface heterogeneity, i.e. an increase in the surface coverage by corrosion products [52,54].

Finally, potentiodynamic measurements performed within this study provided a new set of B constants for AAMs. These constants are higher than the standard parameters developed for OPC, which tend to overestimate corrosion levels [64]. Furthermore, to evaluate the reliability of the new B constant experimentally obtained within this study, the electrochemical mass loss obtained was validated using the gravimetric method according to standard ASTM G1–03 [45], on the same samples on which electrochemical mass loss was measured. Electrochemical mass loss was calculated by employing Faraday's law at various exposure periods by Eq. (4):

$$m_{electrochemical} = \frac{A \times I_{corr} \times t}{n \times F} \tag{4}$$

Where A is the atomic mass of metal (55.85 g/mol for iron), I_{corr} is the intensity of corrosion current in amperes, t is exposure time in seconds, n is the electron number transferred per atom (2 equivalent/mol for iron) and F is the Faraday constant (96,485.33 C/equivalent). The intensity of the corrosion current was calculated using LPR and Tafel intersection method. The data from Fig. 19 indicate that the new B constants provides a better correlation between gravimetric and electrochemical mass loss shows a better fit to the data compared to the value of B= 26 mV as proposed by Andrade and Gonzalez for OPC [64] (dotted lines), and all data are located between the two dashed lines, indicating an acceptable scattering range (a factor of 2 in either direction) as previously defined for OPC samples [41].

Based on the observations presented in this study, it is possible to define several parameters that can be used to distinguish between passive and active condition of steel in AAMs. Table 7 summarizes the index values of E_{corr}, R_{mortar}, n and B for steel in AAMs, and the corresponding risk of corrosion. E_{corr} shows a significant shift to lower potential values compared to the benchmark values presented in ASTM C876 [46], from $-$ 250 $\mathrm{mV_{SCE}}$ to $-$ 400 $\mathrm{mV_{SCE}}$. This difference was already observed by Scott et al. [15] and other authors working on AAMs, and it is mostly caused by the presence of reduced sulfide in blast furnace slag [20]. However, the limit defined for E_{corr} is a conservative consideration that does not take into account the variability of the pH and the availability of oxygen which can lead to values below $-$ 400 mV [58]. Since E_{corr} is highly sensitive to humidity and oxygen availability within the matrix, the R_{mortar} and n values from EIS are proposed as suitable parameters to define the stability of steel in AAMs. Finally, Tafel constants for both conditions of steel are also proposed. It has to be highlighted that these values are proposed based on the experimental results obtained on the set of mixes and exposure conditions analysed in this study. Values proposed are rather conservative, especially the value of corrosion potential. With more research and more experimental values on different sets of mixes, proposed values could be further refined.

Table A1
EIS parameters obtained by fitting the impedance spectra for AAMs in tap water (Ref.) and salt spray chamber (Corr.) after different exposure times.

	Time days	E_{corr} mV	R_{mortar} kΩ cm^2	R_{ct} kΩ cm^2	C_{dl} mF cm^{-2}	n		Time days	E_{corr} mV	R_{mortar} kΩ cm^2	R_{ct} kΩ cm^2	C_{dl} mF cm^{-2}	n
SN3-Ref	28	-300	85	546	22.2	0.60	**SN3-Corr**	28	-300	85	1300	22.6	0.60
	50	-241	92	587	32.2	0.76		50	-271	190	1216	10.7	0.80
	100	-174	168	1079	52.5	0.80		100	-116	188	1201	33.5	0.69
	150	-128	158	1011	55.0	0.79		150	-260	140	900	37.6	0.69
	–	–	–	–		–		200	-317	166	1062	37.0	0.64
	250	-165	213	1362	65.6	0.78		250	-359	268	1691	45.2	0.60
	300	-173	521	3335	38.7	0.78		300	-522	56	358	3.0	0.23
BN3-Ref	28	-236	133	850	26.1	0.64	**BN3-Corr**	28	-236	133	850	26.4	0.64
	50	-354	146	938	24.0	0.71		50	-297	257	1648	30.7	0.71
	100	-1445	172	1103	25.5	0.64		100	-270	304	1948	35.1	0.63
	150	-354	162	1036	15.8	0.42		150	-232	153	980	31.5	0.65
	200	-316	231	1477	18.3	0.41		200	-345	254	1625	32.0	0.67
	250	-346	300	1923	36.3	0.59		250	-427	67	432	12.8	0.46
	300	-182	336	2153	41.2	0.59		300	-701	66	424	3.7	0.36
FN9-Ref	28	-80	1.2	7.0	5.6	0.72	**FN9-Corr**	28	-80	1.2	7.0	5.6	0.72
	50	-355	1.3	7.6	7.1	0.76		50	-312	0.9	5.1	4.5	0.80
	100	-385	1.8	10.9	9.3	0.80		100	-518	0.9	5.5	1.2	0.32
	150	–	–	–		–		150	-523	1.4	8.5	75.0	0.30

5. Conclusion

According to the electrochemical measurements obtained for the three mix designs of AAMs presented in this study, tested in reference and corrosive environments, the main conclusions are as follows:

(I) Corrosion potential, E_{corr}, and polarization resistance, R_p, are strongly influenced by the relative humidity, sulfide content and oxygen availability within the matrix. Nevertheless, long-term corrosion monitoring of reinforced alkali activated materials (AAMs) confirmed that the limiting values for evaluating corrosion process defined for OPC are not acceptable for AAMs. Rather, a lower value of potential of $-400\ \mathrm{mV_{SCE}}$ is proposed as a limiting value for differentiating between passive and active steel in AAM.

(II) Mortar resistance, R_{mortar}, was extracted by EIS fitting and proposed as an indicator of corrosion of reinforcement in AAM. The interest in this parameter is related to possible application as indirect method to evaluate steel condition. The data have shown a visible displacement from the limits defined for OPC and the ability to identify passive and active conditions by observing the values of mortar resistance.

(III) Potentiodynamic polarization showed overall displacement of the B constants from the values defined for OPC. The B value increased with corrosion propagation in systems based on blast furnace slag, where corrosion was monitored from the passive to the active state. When the new proposed B value was used in the calculation, better correlation between electrochemical and gravimetric steel mass loss was obtained. Therefore, use of the proposed B values would allow more precise quantification of corrosion rate based on electrochemical monitoring of steel in AAMs.

CRediT authorship contribution statement

Antonino Runci: Conceptualization, Methodology, Investigation, Formal analysis, Writing – original draft. **John Provis:** Formal analysis, Writing – review & editing, Supervision. **Marijana Serdar:** Conceptualization, Formal analysis, Writing – review & editing, Supervision, Project administration, Funding acquisition.

Declaration of Competing Interest

The authors declare that they have no known competing financial interests or personal relationships that could have appeared to influence the work reported in this paper.

Data Availability

Data will be made available on request.

Acknowledgments

The research presented in this paper was performed within the project DuRSAAM, which has received funding from the European Union's Horizon 2020 research and innovation programme under grant agreement no. 813596. The opinions expressed in this document reflect only the author's view and reflects in no way the European Commission's opinions. The European Commission is not responsible for any use that may be made of the information it contains. Research is also supported by the project "Alternative Binders for Concrete: understanding microstructure to predict durability, ABC", funded by the Croatian Science Foundation under number UIP-05-2017-4767.

Appendix

See Table A1.

References

[1] U.M. Angst, M.R. Geiker, M.C. Alonso, R. Polder, O.B. Isgor, B. Elsener, H. Wong, A. Michel, K. Hornbostel, C. Gehlen, R. François, M. Sanchez, M. Criado, H. Sørensen, C. Hansson, R. Pillai, S. Mundra, J. Gulikers, M. Raupach, J. Pacheco, A. Sagüés, The effect of the steel–concrete interface on chloride-induced corrosion initiation in concrete: a critical review by RILEM TC 262-SCI, Mater. Struct. Constr. 52 (2019), https://doi.org/10.1617/s11527-019-1387-0.

[2] K. Tuutti, Corrosion of Steel in Concrete, Uhlig's Corros. Handb. Third Ed., 1982, pp. 633–647. ⟨https://doi.org/10.1002/9780470872864.ch49⟩.

[3] U. Angst, B. Elsener, C.K. Larsen, Ø. Vennesland, Critical chloride content in reinforced concrete — a review, Cem. Concr. Res 39 (2009) 1122–1138, https://doi.org/10.1016/j.cemconres.2009.08.006.

[4] L. Bertolini, B. Elsener, P. Pedeferri, R. Polder, Corrosion of Steel in Concrete, 2004.

[5] U.M. Angst, O.B. Isgor, C.M. Hansson, A. Sagüés, M.R. Geiker, Beyond the chloride threshold concept for predicting corrosion of steel in concrete, Appl. Phys. Rev. 9 (2022), 011321, https://doi.org/10.1063/5.0076320.

[6] G.H. Koch, M.P.H. Brongers, N.G. Thompson, Y.P. Virmani, J.H. Payer, Corrosion Cost and Preventive, 2002. ⟨https://ntrl.ntis.gov/NTRL/dashboard/searchResults/titleDetail/PB2002106409.xhtml⟩.

[7] U.M. Angst, Challenges and opportunities in corrosion of steel in concrete, Mater. Struct. Constr. 51 (2018) 1–20, https://doi.org/10.1617/s11527-017-1131-6.

[8] S.A. Bernal, J.L. Provis, Durability of alkali-activated materials: pogress and perspectives, J. Am. Ceram. Soc. 97 (2014) 997–1008, https://doi.org/10.1111/jace.12831.

[9] V.K. Gouda, Corrosion and corrosion inhibition of reinforcing steel I. Immersed in alkaline solution, Br. Corros. J. 5 (1970) 198–203, https://doi.org/10.1179/000705970798324450.

[10] P. Ghods, O.B. Isgor, J.R. Brown, F. Bensebaa, D. Kingston, XPS depth profiling study on the passive oxide film of carbon steel in saturated calcium hydroxide solution and the effect of chloride on the film properties, Appl. Surf. Sci. 257 (2011) 4669–4677, https://doi.org/10.1016/j.apsusc.2010.12.120.

[11] R.R. Lloyd, J.L. Provis, J.S.J.Van Deventer, Pore solution composition and alkali diffusion in inorganic polymer cement, Cem. Concr. Res. 40 (2010) 1386–1392, https://doi.org/10.1016/j.cemconres.2010.04.008.

[12] M. Nedeljković, Carbonation mechanism of alkali-activated fly ash and slag materials In view of long-term performance predictions, 2019. ⟨https://doi.org/10.4233/uuid:97b9eabe-159e-43e1–8b35-edc61b1aa682⟩.

[13] S. Mundra, J.L. Provis, Mechanisms of passivation and chloride-induced corrosion of mild steel in sulfide-containing alkaline solutions, J. Mater. Sci. 56 (2021) 14783–14802, https://doi.org/10.1007/s10853-021-06237-x.

[14] J. Shi, J. Ming, W. Sun, Electrochemical behaviour of a novel alloy steel in alkali-activated slag mortars, Cem. Concr. Compos. 92 (2018) 110–124, https://doi.org/10.1016/j.cemconcomp.2018.06.004.

[15] A. Scott, M.G. Alexander, Effect of supplementary cementitious materials (binder type) on the pore solution chemistry and the corrosion of steel in alkaline environments, Cem. Concr. Res. 89 (2016) 45–55, https://doi.org/10.1016/j.cemconres.2016.08.007.

[16] M. Holloway, J.M. Sykes, Studies of the corrosion of mild steel in alkali-activated slag cement mortars with sodium chloride admixtures by a galvanostatic pulse method, Corros. Sci. 47 (2005) 3097–3110, https://doi.org/10.1016/j.corsci.2005.05.035.

[17] F.P. Glasser, K. Luke, M.J. Angus, Modification of cement pore fluid compositions by pozzolanic additives, Cem. Concr. Res. 18 (1988) 165–178, https://doi.org/10.1016/0008-8846(88)90001-4.

[18] M. Criado, S.A. Bernal, P. Garcia-Triñanes, J.L. Provis, Influence of slag composition on the stability of steel in alkali-activated cementitious materials, J. Mater. Sci. 53 (2018) 5016–5035, https://doi.org/10.1007/s10853-017-1919-3.

[19] Y. Wang, R. Chen, J. Hu, Z. Zhang, H. Huang, Y. Ma, J. Wei, Z. Zhang, S. Yin, H. Wang, Q. Yu, Surface characteristics and electrochemical behaviors of passive reinforcing steel in alkali-activated slag, Corros. Sci. 190 (2021), 109657, https://doi.org/10.1016/j.corsci.2021.109657.

[20] S. Mundra, M. Criado, S.A. Bernal, J.L. Provis, Chloride-induced corrosion of steel rebars in simulated pore solutions of alkali-activated concretes, Cem. Concr. Res. 100 (2017) 385–397, https://doi.org/10.1016/j.cemconres.2017.08.006.

[21] R. Chen, J. Hu, Y. Ma, W. Guo, H. Huang, J. Wei, S. Yin, Q. Yu, Characterization of the passive film formed on the reinforcement surface in alkali activated fly ash: Surface analysis and electrochemical evaluation, Corros. Sci. 165 (2019), 108393, https://doi.org/10.1016/j.corsci.2019.108393.

[22] Q. Ma, S.V. Nanukuttan, P.A.M. Basheer, Y. Bai, C. Yang, Chloride transport and the resulting corrosion of steel bars in alkali activated slag concretes, Mater. Struct. Constr. 49 (2016) 3663–3677, https://doi.org/10.1617/s11527-015-0747-7.

[23] M. Babaee, A. Castel, Chloride diffusivity, chloride threshold, and corrosion initiation in reinforced alkali-activated mortars: Role of calcium, alkali, and silicate content, Cem. Concr. Res. 111 (2018) 56–71, https://doi.org/10.1016/j.cemconres.2018.06.009.

[24] H. Zhu, Z. Zhang, Y. Zhu, L. Tian, Durability of alkali-activated fly ash concrete: Chloride penetration in pastes and mortars, Constr. Build. Mater. 65 (2014) 51–59, https://doi.org/10.1016/j.conbuildmat.2014.04.110.

[25] M. Babaee, A. Castel, Water vapor sorption isotherms, pore structure, and moisture transport characteristics of alkali-activated and Portland cement-based binders, Cem. Concr. Res. 113 (2018) 99–120, https://doi.org/10.1016/j.cemconres.2018.07.006.

[26] X. Zhang, K. Long, W. Liu, L. Li, W.J. Long, Carbonation and chloride ions' penetration of alkali-activated materials: a review, Molecules 25 (2020) 1–28, https://doi.org/10.3390/molecules25215074.

[27] A. Runci, M. Serdar, Chloride-induced corrosion of steel in alkali-activated mortars based on different precursors, Materials 13 (5244) (2020) 1–17, https://doi.org/10.3390/ma13225244.

[28] G. Song, Theoretical analysis of the measurement of polarization resistance in reinforced concrete, Cem. Concr. Compos. 22 (2000) 407–415, https://doi.org/10.1016/S0958-9465(00)00040-8.

[29] K. Hornbostel, C.K. Larsen, M.R. Geiker, Relationship between concrete resistivity and corrosion rate - a literature review, Cem. Concr. Compos. 39 (2013) 60–72, https://doi.org/10.1016/j.cemconcomp.2013.03.019.

[30] N. You, J. Shi, Y. Zhang, Corrosion behaviour of low-carbon steel reinforcement in alkali-activated slag-steel slag and Portland cement-based mortars under simulated marine environment, Corros. Sci. 175 (2020), https://doi.org/10.1016/j.corsci.2020.108874.

[31] K. Scrivener, R. Snellings, B. Lothenbach, A Practical Guide to Microstructural Analysis of Cementitious Materials, 2015. ⟨https://doi.org/10.1201/b19074⟩.

[32] J.L. Provis, K. Arbi, S.A. Bernal, D. Bondar, A. Buchwald, A. Castel, S. Chithiraputhiran, M. Cyr, A. Dehghan, K. Dombrowski-Daube, A. Dubey, V. Ducman, G.J.G. Gluth, S. Nanukuttan, K. Peterson, F. Puertas, A. van Riessen, M. Torres-Carrasco, G. Ye, Y. Zuo, RILEM TC 247-DTA round robin test: mix design and reproducibility of compressive strength of alkali-activated concretes, Mater. Struct. 52 (2019) 1–13, https://doi.org/10.1617/s11527-019-1396-z.

[33] G.J.G. Gluth, K. Arbi, S.A. Bernal, D. Bondar, K.D. Ashish, D. Vilma, D. Karl, P. Pipilikaki, S.L.A. Valcke, G. Ye, Y. Zuo, J.L. Provis, RILEM TC 247-DTA round robin test: carbonation and chloride penetration testing of alkali-activated concretes, Mater. Struct. 3 (2020), https://doi.org/10.1617/s11527-020-1449-3.

[34] A. Runci, J. Provis, M. Serdar, Microstructure as key parameter for understanding chloride ingress in alkali-activated mortars, Publ (2022).

[35] Q.D. Nguyen, S. Afroz, A. Castel, Influence of calcined clay reactivity on the mechanical properties and chloride diffusion resistance of limestone calcined clay cement (LC3) Concrete, J. Mar. Sci. Eng. 8 (2020) 1–14.

[36] A. Runci, M. Serdar, Effect of curing time on the chloride diffusion of alkali-activated slag, Case Stud. Constr. Mater. 16 (2022), https://doi.org/10.1016/j.cscm.2022.e00927.

[37] I. Ismail, S.A. Bernal, J.L. Provis, R. San Nicolas, D.G. Brice, A.R. Kilcullen, S. Hamdan, J.S.J.Van Deventer, Influence of fly ash on the water and chloride permeability of alkali-activated slag mortars and concretes, Constr. Build. Mater. 48 (2013) 1187–1201, https://doi.org/10.1016/j.conbuildmat.2013.07.106.

[38] C. Christodoulou, C.I. Goodier, S.A. Austin, J. Webb, G. Glass, On-site transient analysis for the corrosion assessment of reinforced concrete, Corros. Sci. 62 (2012) 176–183, https://doi.org/10.1016/j.corsci.2012.05.014.

[39] C. Andrade, C. Alonso, F.J. Molina, Cover cracking as a function of bar corrosion: Part I-Experimental test, Mater. Struct. 26 (1993) 453–464, https://doi.org/10.1007/BF02472805.

[40] T. El Maaddawy, K. Soudki, A model for prediction of time from corrosion initiation to corrosion cracking, Cem. Concr. Compos. 29 (2007) 168–175, https://doi.org/10.1016/j.cemconcomp.2006.11.004.

[41] C. Andrade, C. Alonso, Corrosion rate monitoring and on-site, Constr. Build. Mater. 10 (1996) 315–328.

[42] F. Mansfeld, Discussion: electrochemical techniques for studying corrosion of reinforcing steel: limitations and advantages, Corrosion 61 (2005) 739–742, https://doi.org/10.5006/1.3281682.

[43] Z.T. Chang, B. Cherry, M. Marosszeky, Polarisation behaviour of steel bar samples in concrete in seawater. Part 1: Experimental measurement of polarisation curves of steel in concrete, Corros. Sci. 50 (2008) 357–364, https://doi.org/10.1016/j.corsci.2007.08.009.

[44] C. Andrade, C. Alonso, J. Gulikers, R. Polder, R. Cigna, Vennesland, M. Salta, A. Raharinaivo, B. Elsener, Test methods for on-site corrosion rate measurement of steel reinforcement in concrete by means of the polarization resistance method, Mater. Struct. Constr. 37 (2004) 623–643, https://doi.org/10.1617/13952.

[45] ASTM G1/03 - Standard Practice for Preparing, Cleaning, and Evaluating Corrosion Test, 1999. ⟨https://doi.org/10.1520/G0001–03R11.2⟩.

[46] ASTM C 876/09 - Standard Test Method for Half-Cell Potentials of Uncoated Reinforcing Steel in concrete, 1999.

[47] U.M. Angst, B. Elsener, C.K. Larsen, Ø. Vennesland, Chloride induced reinforcement corrosion: Electrochemical monitoring of initiation stage and chloride threshold values, Corros. Sci. 53 (2011) 1451–1464, https://doi.org/10.1016/j.corsci.2011.01.025.

[48] B. Elsener, C. Andrade, J. Gulikers, R. Polder, M. Raupach, Half-cell potential measurements - Potential mapping on reinforced concrete structures, Mater. Struct. Constr. 36 (2003) 461–471, https://doi.org/10.1617/13718.

[49] A.S. Castela, B.S. Da Fonseca, R.G. Duarte, R. Neves, M.F. Montemor, Influence of unsupported concrete media in corrosion assessment for steel reinforcing concrete by electrochemical impedance spectroscopy, Electrochim. Acta 124 (2014) 52–60, https://doi.org/10.1016/j.electacta.2013.11.157.

[50] F. Tang, G. Chen, R.K. Brow, Chloride-induced corrosion mechanism and rate of enamel- and epoxy-coated deformed steel bars embedded in mortar, Cem. Concr. Res. 82 (2016) 58–73, https://doi.org/10.1016/j.cemconres.2015.12.015.

[51] D.A. Koleva, J.H.W. de Wit, K. van Breugel, L.P. Veleva, E. van Westing, O. Copuroglu, A.L.A. Fraaij, Correlation of microstructure, electrical properties and electrochemical phenomena in reinforced mortar. Breakdown to multi-phase interface structures. Part II: Pore network, electrical properties and electrochemical response, Mater. Charact. 59 (2008) 801–815, https://doi.org/10.1016/j.matchar.2007.06.016.

[52] D.M. Bastidas, Interpretation of impedance data for porous electrodes and diffusion processes, Corrosion 63 (2007) 515–521, https://doi.org/10.5006/1.3278402.

[53] M. Serdar, L.V. Žulj, D. Bjegović, Long-term corrosion behaviour of stainless reinforcing steel in mortar exposed to chloride environment, Corros. Sci. 69 (2013) 149–157, https://doi.org/10.1016/j.corsci.2012.11.035.

[54] M. Farcas, N.P. Cosman, D.K. Ting, S.G. Roscoe, S. Omanovic, A comparative study of electrochemical techniques in investigating the adsorption behaviour of fibrinogen on platinum, J. Electroanal. Chem. 649 (2010) 206–218, https://doi.org/10.1016/j.jelechem.2010.04.004.

[55] D. Bondar, Q. Ma, M. Soutsos, M. Basheer, J.L. Provis, S. Nanukuttan, Alkali activated slag concretes designed for a desired slump, strength and chloride diffusivity, Constr. Build. Mater. 190 (2018) 191–199, https://doi.org/10.1016/j.conbuildmat.2018.09.124.

[56] J. Shi, M. Wu, J. Ming, Long-term corrosion resistance of reinforcing steel in alkali-activated slag mortar after exposure to marine environments, Corros. Sci. 179 (2021), https://doi.org/10.1016/j.corsci.2020.109175.

[57] M. Criado, S. Martínez-Ramirez, S. Fajardo, P.P. Gõmez, J.M. Bastidas, Corrosion rate and corrosion product characterisation using Raman spectroscopy for steel embedded in chloride polluted fly ash mortar, Mater. Corros. 64 (2013) 372–380, https://doi.org/10.1002/maco.201206714.

[58] M. Criado, J.L. Provis, Alkali activated slag mortars provide high resistance to chloride-induced corrosion of steel, Front. Mater. 5 (2018), https://doi.org/10.3389/fmats.2018.00034.

[59] M. Stefanoni, U.M. Angst, B. Elsener, Kinetics of electrochemical dissolution of metals in porous media, Nat. Mater. 18 (2019) 942–947, https://doi.org/10.1038/s41563-019-0439-8.

[60] J. Hu, D.A. Koleva, J.H.W. De Wit, H. Kolev, K. Van Breugel, Corrosion performance of carbon steel in simulated pore solution in the presence of micelles, J. Electrochem. Soc. 158 (2011) 76–87, https://doi.org/10.1149/1.3534796.

[61] C. Andrade, M. Keddam, X.R. Nóvoa, M.C. Perez, C.M. Rangel, H. Takenouti, Electrochemical behaviour of steel rebars in concrete: influence of environmental factors and cement chemistry, Electrochim. Acta 46 (2001) 3905–3912.

[62] C. Monticelli, A. Frignani, A. Balbo, F. Zucchi, Influence of two specific inhibitors on steel corrosion in a synthetic solution simulating a carbonated concrete with chlorides, Mater. Corros. 62 (2011) 178–186, https://doi.org/10.1002/maco.201005764.

[63] G.J. Brug, A.L.G. van den Eeden, M. Sluyters-Rehbach, J.H. Sluyters, The analysis of electrode impedances complicated by the presence of a constant phase element, J. Electroanal. Chem. 176 (1984) 275–295, https://doi.org/10.1016/S0022-0728(84)80324-1.

[64] C. Andrade, J.A. González, Quantitative measurements of corrosion rate of reinforcing steels embedded in concrete using polarization resistance measurements, Mater. Corros. 29 (1978) 515–519, https://doi.org/10.1002/maco.19780290804.

[65] Z.T. Chang, B. Cherry, M. Marosszeky, Polarisation behaviour of steel bar samples in concrete in seawater. Part 2: A polarisation model for corrosion evaluation of steel in concrete, Corros. Sci. 50 (2008) 3078–3086, https://doi.org/10.1016/j.corsci.2008.08.021.

[66] Q.D. Nguyen, A. Castel, Reinforcement corrosion in limestone flash calcined clay cement-based concrete, Cem. Concr. Res. 132 (2020), https://doi.org/10.1016/j.cemconres.2020.106051.

[67] P. Garcés, M.C. Andrade, A. Saez, M.C. Alonso, Corrosion of reinforcing steel in neutral and acid solutions simulating the electrolytic environments in the micropores of concrete in the propagation period, Corros. Sci. 47 (2005) 289–306, https://doi.org/10.1016/j.corsci.2004.06.004.

[68] C. Andrade, Reliability analysis of corrosion onset: initiation limit state, J. Struct. Integr. Maint. 2 (2017) 200–208, https://doi.org/10.1080/24705314.2017.1388693.

[69] K. Hornbostel, B. Elsener, U.M. Angst, C.K. Larsen, M.R. Geiker, Limitations of the use of concrete bulk resistivity as an indicator for the rate of chloride-induced macro-cell corrosion, Struct. Concr. 18 (2017) 326–333, https://doi.org/10.1002/suco.201500141.

[70] C. Andrade, Design and evaluation of service life through concrete electrical resistivity, Rev. Alconpat. 8 (2018) 264–279, https://doi.org/10.21041/ra.v8i3.349.